

# Double Active Layers Constructed with Halide Perovskite and Quantum Dots for Broadband Photodetection

Ruiqi Guo, Chunxiong Bao, Feng Gao,\* and Jianjun Tian\*

Herein, solution-processed, high-performance broadband (300–1100 nm) photodetectors based on double active layers incorporating narrow-bandgap CuInSe<sub>2</sub> (CISe) quantum dots (QDs) and halide perovskite are devised. The CISe QDs/perovskite film as the photoactive layer boosts the photocurrent and suppresses dark current. Due to the joint light absorption effect of CISe QDs and halide perovskite, the photoelectric conversion capacity is improved. Furthermore, CISe QDs as an electron-blocking layer can effectively block electrons to the hole transport layer and reduce the thermal noise. The optimized photodetector exhibits responsivity over 150 mA W<sup>-1</sup> in the visible and more than 20 mA W<sup>-1</sup> in the near-infrared (800–1000 nm) ranges, specific detectivity of more than  $7.0 \times 10^{12}$  Jones in the visible region and  $7.7 \times 10^{11}$  Jones in the near-infrared region, a transient response time of 277 ns with the active area of 0.013 cm<sup>2</sup>, and a linear dynamic range of ≈75 dB. Importantly, the CISe QDs layer makes the perovskite denser and more hydrophobic, thus improves the environmental and thermal stability of the detector, even extends the working temperature to exceeding 150 °C. The design concept and the considerable performance of this novel device provide a reference value for polychromatic light detection.

## 1. Introduction

Lead halide perovskite has been widely studied in ultraviolet (UV)–vis photodetectors due to its excellent carrier mobility (1–250 cm<sup>2</sup> V<sup>-1</sup> s<sup>-1</sup>), strong defect tolerance, and large absorption coefficient ( $\sim 10^5$  cm<sup>-1</sup>).<sup>[1–4]</sup> Meanwhile, the perovskite-based photodetector exhibits high specific detectivity ( $D^*$ ), low noise equivalent power (NEP), and fast response speed.<sup>[5–7]</sup> Despite the great development, it is almost a fantasy story for lead halide perovskite photodetectors to achieve a broadband response up to the near-infrared region. Broadband photodetectors with the

response from UV to near-infrared ranges play an important role in light communication, wide spectrum switching, and information storage.<sup>[8]</sup> Although the introduction of the Sn element can adjust the bandgap to the near-infrared region,<sup>[9]</sup> the problem of the inherent material instability (Sn<sup>2+</sup> is oxidized to Sn<sup>4+</sup>) hinders their development. Furthermore, the response range cannot reach more than 1000 nm wavelength.

Colloidal quantum dot (QD)-based photodetectors emerge as a promising alternative to traditional detectors, because of their several merits, that is, flexible bandgap, excellent stability, and low-cost solution process manufacturing.<sup>[10–12]</sup> Colloidal CuInSe<sub>2</sub> (CISe) QD with narrow bandgap is considered a candidate for broadband response photodetector because of its high absorption coefficient ( $\approx 10^5$  cm<sup>-1</sup>), superior stability, and broadband response (UV to near-infrared).<sup>[13–18]</sup> However, choosing an appropriate charge transport layer and preparing a sufficiently

thick active layer are the challenges for CISe QD-based photodetectors. These problems lead to an unsatisfactory response of CISe QD-based photodetectors in the visible light region compared to traditional detectors. Therefore, a novel double-active-layer photodetector (DALPD) based on lead halide perovskite and CISe QD is proposed. In DALPD, the halide perovskite displays superior response ability in the visible light region, while CISe QDs provides light response in the near-infrared region, realizing the broadband response from UV to the near-infrared region under the synergistic effect.

Herein, we fabricate DALPD composed of metal lead halide perovskite and CISe QDs by the solution-processing method. The resulting DALPD shows broadband response from 300 to 1100 nm, fast response speed (277 ns with the active area is 0.013 cm<sup>2</sup>), and appreciable linear dynamic range (75.16 dB). Moreover, the DALPD also exhibits considerable environmental stability (300 h) and outstanding thermal stability (150 °C) under unencapsulated conditions.

## 2. Results and Discussions

We design a novel DALPD with configuration of FTO/polymer poly-(3,4-ethylenedioxothiophene):poly(styrene sulfonate) (PEDOT:PSS)/CISe QDs/perovskite CH<sub>3</sub>NH<sub>3</sub>PbI<sub>3</sub>

R. Guo, Prof. J. Tian  
Institute for Advanced Materials and Technology  
University of Science and Technology  
Beijing 100083, China  
E-mail: tianjianjun@mater.ustb.edu.cn

Dr. C. Bao, Prof. F. Gao  
Department of Physics, Chemistry, and Biology (IFM)  
Linköping University  
Linköping SE-58183, Sweden  
E-mail: feng.gao@liu.se

The ORCID identification number(s) for the author(s) of this article can be found under <https://doi.org/10.1002/adom.202000557>.

DOI: 10.1002/adom.202000557

( $\text{MAPbI}_3$ )/[6,6]-phenyl-C61-butyric acid methyl ester (PCBM)/silver (Ag) as shown in **Figure 1a**. The double-active-layer structure of the DALPD is confirmed by the cross-sectional scanning electron microscopy (SEM) image in **Figure 1b**. Each functional layer is clearly observed, which appears to be highly dense. The energy levels of each layer<sup>[14,19]</sup> in the photodetector are shown in **Figure 1c**. The electrons are transferred via PCBM to the Ag electrode, whereas the holes are transferred by PEDOT:PSS to the ITO. The CISe QD layer not only absorbs light and generates electron-hole pairs but also transports the holes and blocks the electrons from the perovskite layer to the HTL due to gradient energy alignment. The valence band position of CISe QD is slightly deeper than the highest occupied molecular orbital (HOMO) energy level of PEDOT:PSS, which could boost holes transfer and extraction.<sup>[20,21]</sup> Similarly, perovskite can extract electrons from CISe QD layer. Moreover, narrow-bandgap CISe QDs, as a potential near-infrared absorber, extends the photoresponse range of perovskite photodetector. In general, the design of

the double-active-layer structure is beneficial for the carriers' transmission and broadband response. **Figure 1d,e** shows the scanning transmission electron microscopy (STEM) image of CISe QDs and top-view SEM of the perovskite, respectively. Insets in **Figure 1d,e** show the crystal structure of CISe QDs (chalcopyrite structure) and perovskite (cubic structure).

**Figure 1f,g** shows the absorption and photoluminescence (PL) spectra of CISe QD and perovskite films, respectively. The absorption and PL emission peaks of CISe QDs film are located at 1098 and 1136 nm, respectively. For perovskite film, the absorption edge only extends to 780 nm and the PL emission peak is at 773 nm. As expected, the double-active-layer film has a superposition of both the absorption and PL spectra of CISe QDs and perovskite, as shown in **Figure 1h**.

The space-charge-limited current (SCLC) would directly evaluate the trap density ( $n_{\text{trap}}$ ) of the active films.<sup>[22,23]</sup> The typical dark current density ( $J_d$ )–voltage (V) characteristics of the electron-only device with an architecture of FTO/compact  $\text{TiO}_2$ /active layer/PCBM/Ag are measured, as shown in **Figure 2**.

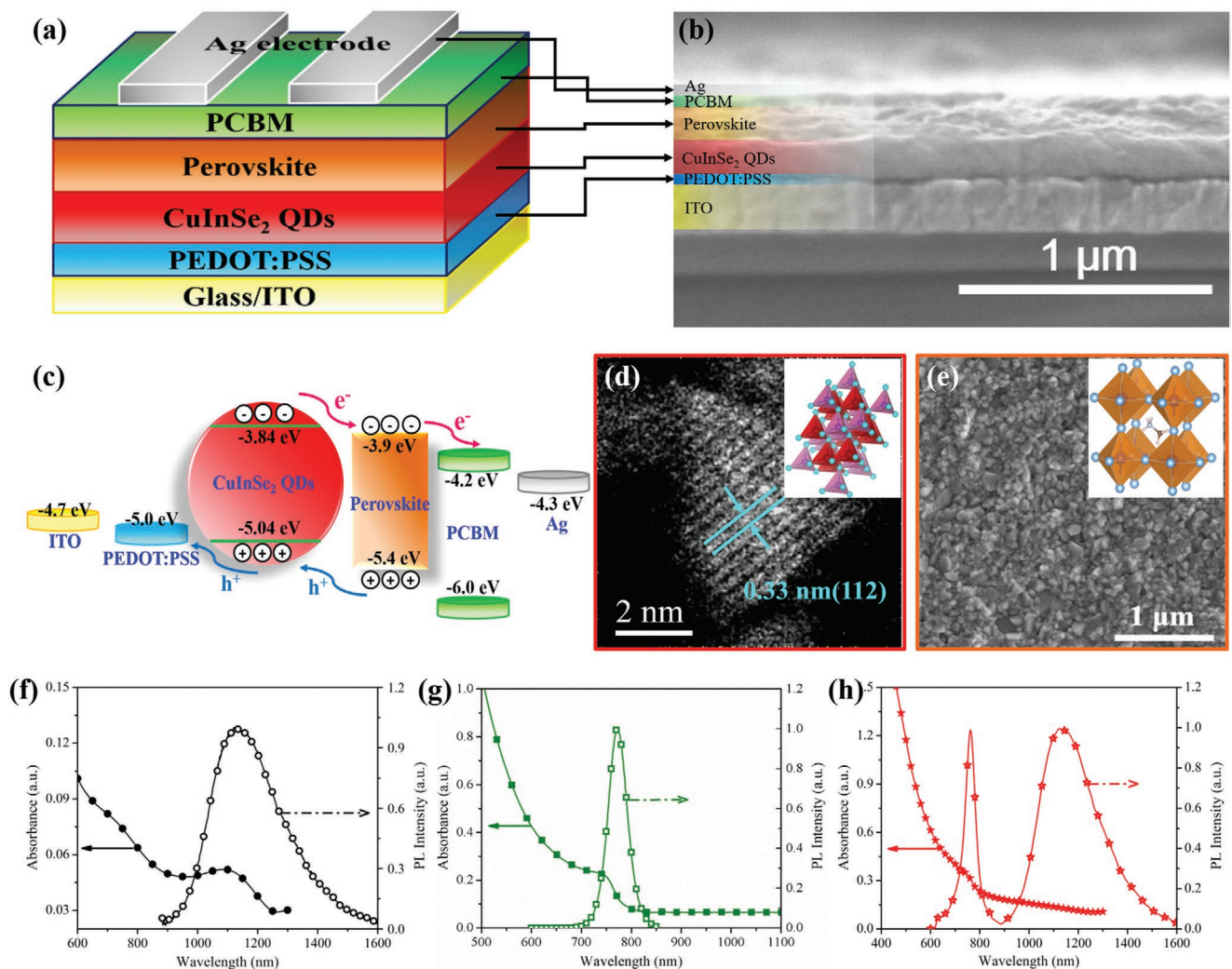


**Figure 1.** a) The architecture structure and b) the cross-sectional SEM image of the DALPD. c) The energy band diagram of the DALPD. d) The STEM image of CISe QDs. Inset shows the structure of CISe QDs. e) Surface SEM image of perovskite. Inset shows the structure of perovskite. The absorption and PL spectra of f) CISe QD film, g) perovskite film, and h) CISe QD/perovskite film.

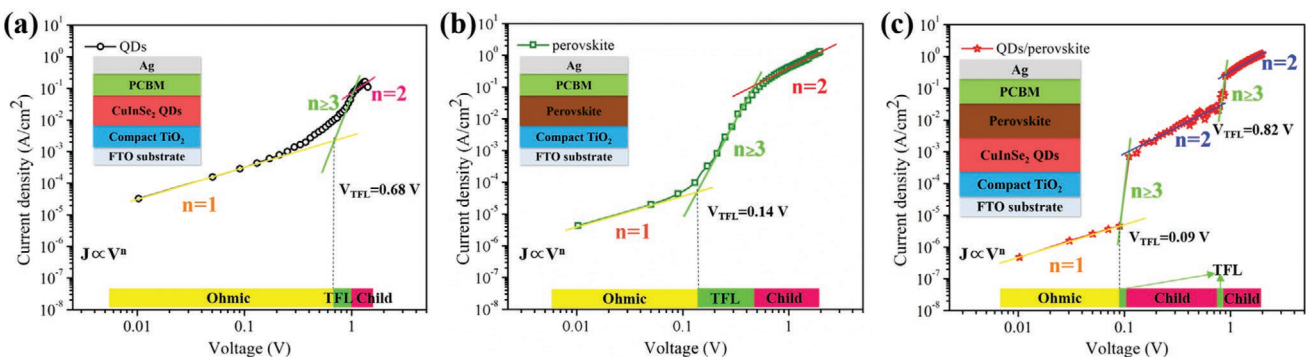


**Figure 2.** Space-charge-limited current of FTO/TiO<sub>2</sub>/active layer/PCBM/Ag devices with the a) CISe QD film, b) perovskite film, and c) double active layers.

Figure 2a,b shows the SCLC results of the devices with a single active layer. At the lower bias voltage, the linear relationship between the current density and voltage is corresponding to the ohmic conduction. As the voltage increases, the current rises rapidly, suggesting the trap-filled limit (TFL). The intersection voltage between the ohmic conduction and trap-filled regime is the trap-limit voltage ( $V_{\text{TFL}}$ ). The  $V_{\text{TFL}}$  values of CISe QD film and perovskite film are 0.68 and 0.14 V, respectively. Herein, the  $n_{\text{trap}}$  can be expressed by the following formula<sup>[23–27]</sup>

$$n_{\text{trap}} = \frac{2\varepsilon\epsilon_0 V_{\text{TFL}}}{eL} \quad (1)$$

here,  $\varepsilon$  is the relative dielectric constant of CISe QDs or perovskite,  $\epsilon_0$  is the vacuum permittivity,  $e$  is the elementary charge, and  $L$  is the thickness of the active film. The  $n_{\text{trap}}$  of CISe QD film and perovskite film can be calculated as  $4.0 \times 10^{16}$  and  $2.7 \times 10^{16} \text{ cm}^{-3}$ , respectively. After that, the current density increases quadratically as the voltage increases, which is the child's square region. Similarly, we also evaluated the SCLC on the device with a double-active-layer film composed of CISe QDs and perovskite, as shown in Figure 2c. Surprisingly, the curve is divided into five stages, instead of the traditional three regions. The first inflection point  $V_{\text{TFL}}$  (0.09 V) is determined by perovskite layer. The corresponding  $n_{\text{trap}}$  is  $1.8 \times 10^{16} \text{ cm}^{-3}$ , which is much lower than the only perovskite-based device. This may be attributed to the defects passivated by QDs layer. After that, the defects in the perovskite layer are quickly filled by charges. When the equilibrium is reached, the traps within the CISe QDs layer are filled in sequence, with corresponding  $V_{\text{TFL}}$  of 0.82 V and  $n_{\text{trap}}$  of  $4.8 \times 10^{16} \text{ cm}^{-3}$ . The SCLC results directly reflect the lower defect density and faster trap-filling capability of the double active layer.

Figure 3a displays the typical photocurrent density ( $J_L$ ) and  $J_d$  versus voltage curves of the devices. The photocurrent density was measured under an illumination density of  $100 \text{ mW cm}^{-2}$ . Compared with the perovskite device, the DALPD remains substantially constant at a reverse bias close to 0 V, indicating that the electrons and holes can be efficiently extracted at 0 V bias. The  $J_L$  of the perovskite detector and DALPD under 0 bias voltage are 3.8 and  $7.9 \text{ mA cm}^{-2}$ , respectively, suggesting that the combine action of CISe QDs and perovskite improved the light absorption capacity.  $J_d$  is an important factor that affects

the sensitivity and detectivity of the photodetector, as well as the key element to achieve high-performance detectors. The  $J_d$  values of the perovskite photodetector and DALPD under 0 bias voltage are  $3.2 \times 10^{-6}$  and  $8.4 \times 10^{-7} \text{ A cm}^{-2}$ , respectively, indicating that the DALPD has fewer defects and strong anti-noise capability.

Responsivity ( $R$ ) and  $D^*$  are two other important technical indexes to evaluate the quality of photodetectors. The  $R$  spectra are shown in Figure 3b. The  $R$  spectrum of DALPD shows a peak of  $193 \text{ mA W}^{-1}$  at 580 nm, which is higher than that of perovskite single-layer detector ( $115 \text{ mA W}^{-1}$ ). It is attributed to the coabsorption of CISe QDs and perovskite. The DALPD shows a broadband response up to 1100 nm due to the light absorption of CISe QDs, which compensates the response of perovskite materials after 780 nm.

In order to better analyze the  $D^*$  of the DALPD, the noise current was accurately recorded at different frequencies, as shown in Figure 3c inset. The noise current of the DALPD is  $8.7 \text{ fA Hz}^{-1/2}$  at high frequency (700 Hz), indicating that the main source of total noise is the device rather than flicker noise caused by charge capture.<sup>[28]</sup> Based on the noise current and  $R$ , the  $D^*$  ( $D^* = \frac{R\sqrt{A}}{i_n}$ , where  $A$  is the active area and  $i_n$  is the noise current) of the DALPD can be calculated to be greater than  $7.0 \times 10^{12} \text{ cm W}^{-1} \text{ Hz}^{1/2}$  at 580 nm and  $7.7 \times 10^{11} \text{ cm W}^{-1} \text{ Hz}^{1/2}$  at 850 nm, respectively. The noise current used to determine the  $D^*$  is the lowest noise current at 700 Hz, and the corresponding NEP of the DALPD is  $4.5 \times 10^{-14} \text{ W Hz}^{-1/2}$  at 580 nm and  $4.1 \times 10^{-13} \text{ W Hz}^{-1/2}$  at 850 nm, respectively. The parameter values exhibited by this novel double-active-layer broadband photodetector imply that the DALPD has potential applications in both visible and near-infrared regions.

Linear dynamic range (LDR) is the crucial performance metrics for photodetectors and can be calculated as<sup>[1,3,11,29–31]</sup>

$$\text{LDR} = 20 \log \frac{J_{\text{light}}}{J_{\text{dark}}} \quad (2)$$

where the  $J_{\text{light}}$  is the photocurrent density measured at  $1 \text{ mW cm}^{-2}$ . Figure 3d shows the LDR of the devices. The LDR of the DALPD is 75.16 dB, which is larger than the perovskite device (51.50 dB). Inset of Figure 3d exhibits the photo-to-dark current ratio ( $\alpha$ ) of the perovskite device and DALPD between 0.01 and  $1 \text{ mW cm}^{-2}$ . The DALPD displays  $\alpha$  of 4056, which is

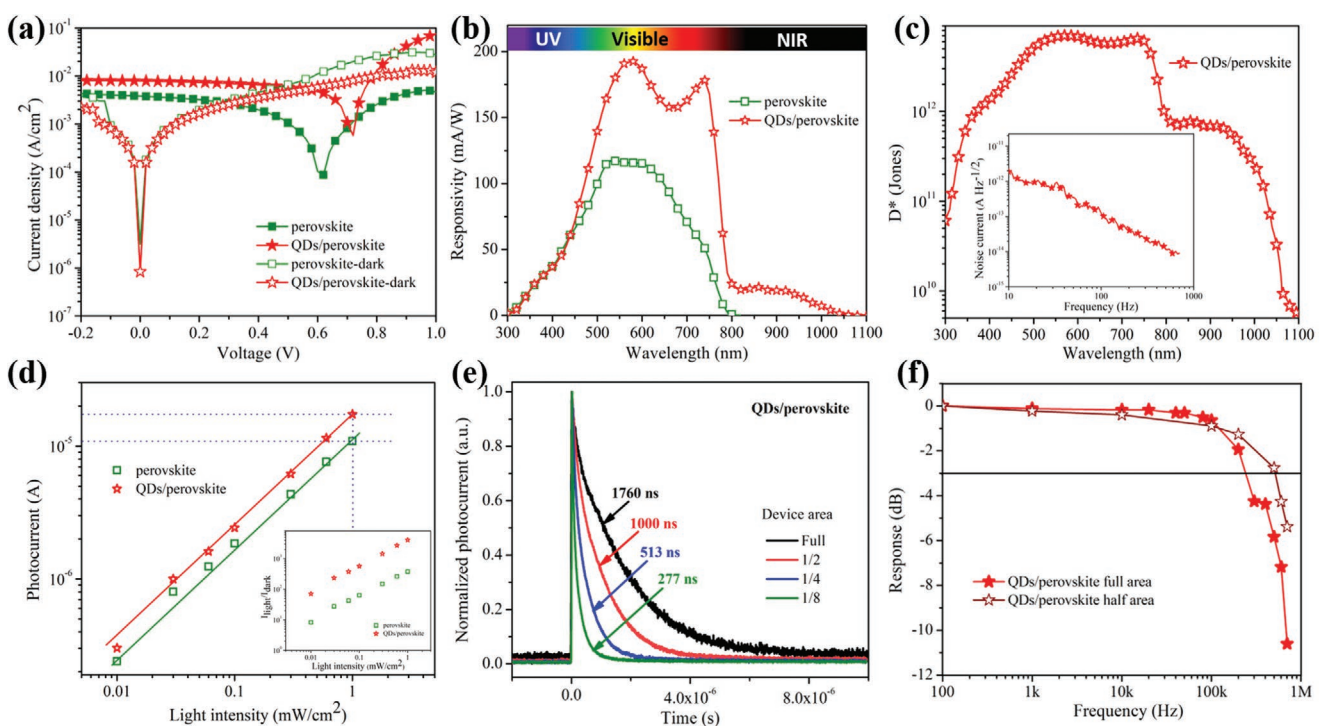


**Figure 3.** a) Current density–voltage ( $J$ – $V$ ) curves of the perovskite photodetector and DALPD in dark and under an illumination intensity of  $100 \text{ mW cm}^{-2}$ . b) Responsivity and c) specific detectivity spectra at  $0 \text{ V}$  bias voltage of photodetectors. Inset is the noise current spectra of the DALPD. d) Dependence of excitation intensity on the photocurrent. Inset is the photo-to-dark current ratio ( $\alpha$ ) of the perovskite device and DALPD between  $0.01$  and  $1 \text{ mW cm}^{-2}$ . e) Transient photocurrent curves of DALPD with different active areas from  $0.013$  to  $0.10 \text{ cm}^2$ . f) The frequency response of the DALPD.

much larger than the value of the perovskite device (376). The higher LDR and  $\alpha$  indicate the DALPD has the capability to monitor a wider light intensity range with weaker background noise.

Figure 3e shows the transient photocurrent (TPC) of the DALPD with different areas. The results of single exponential fitting for TPC show that the response time of the DALPD with the active area of  $0.1 \text{ cm}^2$  is determined to  $1760 \text{ ns}$ . The response time decreases with decreasing active area and achieves a value of  $277 \text{ ns}$  at active area of  $0.013 \text{ cm}^2$ , indicating that the response time is mainly dominated by the resistance-capacitance (RC) constant. Figure 3f shows the frequency response of the DALPD. The full-active-area ( $0.1 \text{ cm}^2$ ) device shows a  $3 \text{ dB}$  cut-off frequency ( $f_{-3 \text{ dB}}$ ) of  $241 \text{ kHz}$  and the half area ( $0.05 \text{ cm}^2$ ) device shows a  $f_{-3 \text{ dB}}$  of  $515 \text{ kHz}$ .

We investigate the response reliability of unencapsulated photodetectors under different illumination conditions. Figure 4a shows the response of the fresh photodetectors under various illumination ( $8, 31, 54, 77$ , and  $100 \text{ mW cm}^{-2}$ ) switched on and off repeatedly. Under any light intensity conditions, DALPD shows excellent photocurrents, which indicates that the CISe QDs layer promotes the light absorption of the photodetector. With the increase of the light intensity, all CISe QDs, perovskite, and DALPD devices show a steady increase in current. When the light power intensity is increased from  $8$  to  $100 \text{ mW cm}^{-2}$ , the photocurrent of DALPD increased by  $1100\%$ . The current density downtrend of the device under  $100 \text{ mW cm}^{-2}$  is attributed to surface defects of QDs that would

cause charge accumulation.<sup>[24,32]</sup> Different current densities of the devices under various light intensities indicate that the devices contain different light obligation. At the light power intensity of  $100 \text{ mW cm}^{-2}$ , the photocurrent of DALPD is  $2.5$  times that of the perovskite device (Figure 4b), which shows that DALPD has stronger optical sensitivity.

Figure 4c shows the light response of the devices under the illumination of near-infrared of  $850 \text{ nm}$  ( $0.4, 1.6, 2.7, 3.8$ , and  $5.0 \text{ mW cm}^{-2}$ ). Under this irradiation condition, the photocurrent of the perovskite device is almost  $0$ , which is due to the limitation of the light absorption of perovskite (Figure 1h). However, both CISe QDs and DALPD devices show obvious optical response under any light power intensity, which further demonstrates the response of the DALPD in the near-infrared region generated by CISe QDs. Figure 4d summarizes the response of the detectors under different  $850 \text{ nm}$  light intensities, indicating that the CISe QDs not only provide photocurrent as a light absorption layer but also expand the response range to the near-infrared region.

We investigate the long-term stability of the devices in air condition without encapsulation. Since the photocurrent is directly related to the responsivity, the stability of the device is studied by monitoring the photocurrent parameter changes over  $300 \text{ h}$ . Figure 5a shows the photocurrent evolution of the devices under an illumination intensity of  $100 \text{ mW cm}^{-2}$ . Initially, the DALPD exhibits superior photocurrent density ( $9.28 \text{ mA cm}^{-2}$ ) compared to the perovskite device ( $2.71 \text{ mA cm}^{-2}$ ). During the first  $132 \text{ h}$ , the photocurrent density of the perovskite photodetector

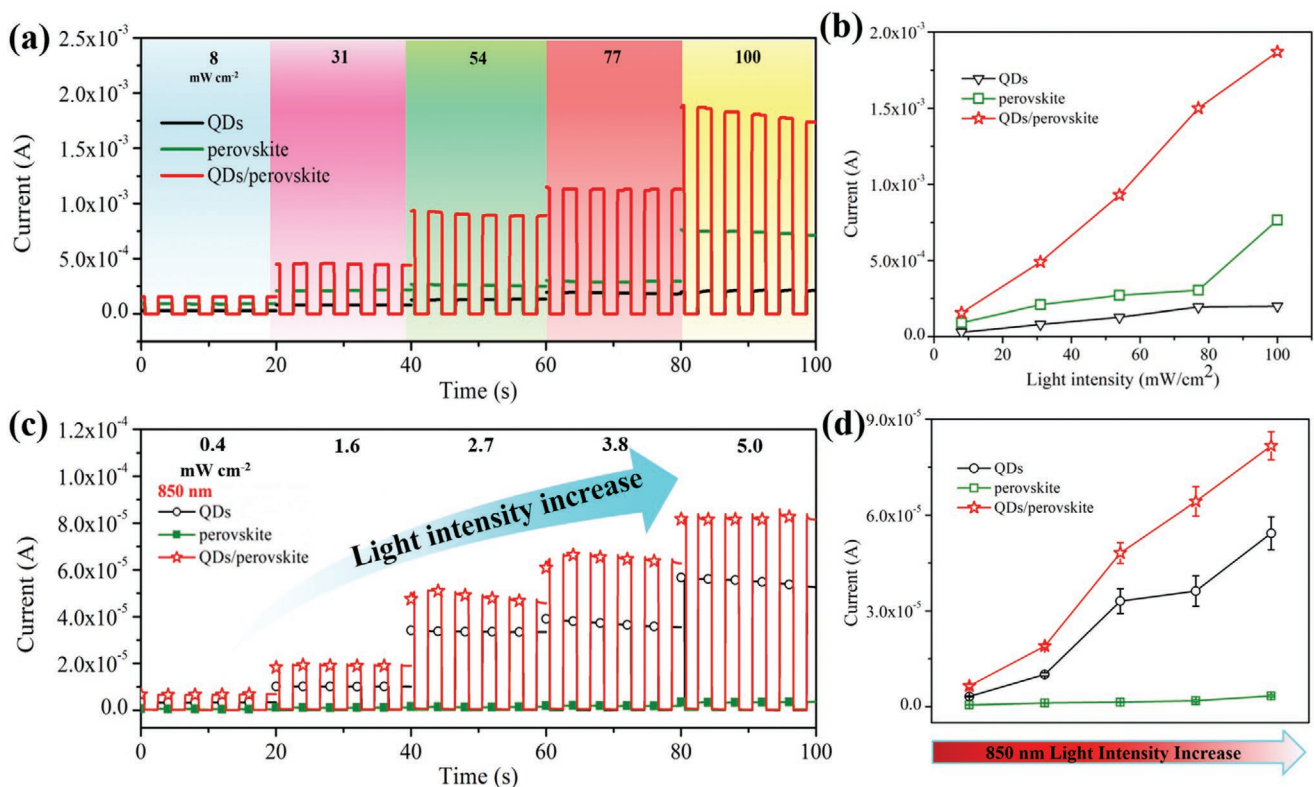


**Figure 4.** a) Time-dependent response of photodetectors based on CISe QDs, perovskite, and DALPD (at 0 bias voltage) under different light power intensities of 8, 31, 54, 77, and 100 mW cm<sup>-2</sup>. b) The relationship between the current and light intensity of the devices based on CISe QDs, perovskite, and DALPD. c) Time-dependent response of fresh photodetectors based on CISe QDs, perovskite, and DALPD (at 0 bias voltage) to 850 nm on/off modulated light. d) The relationship between the current and the 850 nm modulated light intensity of devices based on CISe QDs, perovskite, and DALPD in the air without encapsulation.

has a significant attenuation (52.8%). However, the DALPD still retains more than 80% of the initial current value. Here, we believe that p-type CISe QDs not only block electrons, but also protect the organic HTL, thereby improving the stability of the photodetector. Subsequently, for the next 168 h, the current density of the DALPD remains almost stable at 73.1% of the initial current density value, while the photocurrent density of the perovskite detector decreases by 34.0% of the initial value. The contact angle of the perovskite surfaces based on PEDOT:PSS and PEDOT:PSS/CISe QDs is investigated, as shown in Figure 5b. The contact angle of the PEDOT:PSS/CISe QDs/perovskite film is 57°, which is much higher than that of PEDOT:PSS/perovskite film (26°), suggesting that the presence of the CISe QDs layer makes the perovskite more hydrophobic, thus improving the stability of the device. This would be attributed to the improvement of the perovskite film quality based on the QDs layer.<sup>[17]</sup>

Besides, we also carry out the thermal stability test of the devices through heating the devices for 10 min at different temperatures (30–150 °C) as shown in Figure 5c,d. The responsivity of the perovskite device experiences a rapid decay to 4.8% of its initial value, while the responsivity of the DALPD still maintains 97.6% of the original value. We also find that the responsivity of the DALPD shows a slight increase with increasing temperature below 110 °C. It is attributed to the outstanding thermal stability of CISe QDs. Under high-temperature processing,

the responsivity of the DALPD in the near-infrared region is slightly improved, which is attributed to the good high-temperature resistance of CISe QDs, as shown in Figure 5d. In general, the introduction of CISe QDs into the perovskite photodetector not only promotes the crystallization of the perovskite layer, thereby improves the hydrophobicity, but also improves the thermal stability of the DALPD.

### 3. Conclusions

We designed and demonstrated a stable DALPD based on a double active layer of perovskite and CISe QDs, which shows broadband response from the UV to near-infrared. In DALPD, perovskite exerts its superior light response in the UV to the visible region, and the CISe QDs provide the light response in the near-infrared region. Furthermore, the introduction of CISe QDs not only facilitates the correct separation of carriers but also improves the air stability and thermal stability of the photodetector. The optimized DALPD exhibits broadband continuous response from 300 to 1100 nm, suppressed dark current, high light sensitivity, fast response speed, considerable air stability, and outstanding thermal stability over 150 °C. The successful development of the DALPD and its impressive performance would open a new window for the design of polychromatic detectors.

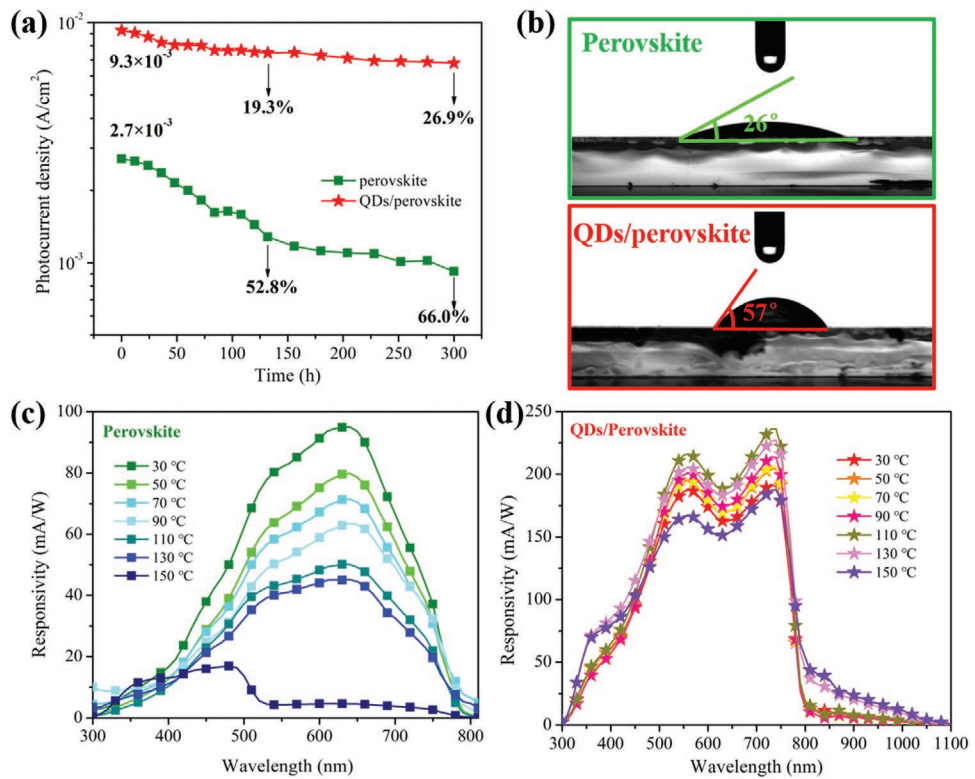


**Figure 5.** a) Time stability of the unencapsulated perovskite photodetector and DALPD. b) Contact angle measurements of a water droplet on the top of the PEDOT:PSS/perovskite and PEDOT:PSS/QDs/perovskite. Thermal stability of the unencapsulated c) pure perovskite photodetector and d) DALPD.

#### 4. Experimental Section

**CISe QDs Synthesis and  $\text{CH}_3\text{NH}_3\text{PbI}_3$  Film Preparation:** A total of 0.1 mmol Cul, 0.1 mmol  $\text{In(OAc)}_3$ , 2 mL OAm, and 2 mL ODE were loaded into a three-necked flask. The temperature was increased to 110 °C after converting all of the air to nitrogen under vacuum for 5 min. The system was heated to 200 °C followed by injection of the Se precursor (0.3 mmol Se powder in 0.3 mL DPP and 0.5 mL OAm). After 5 min, the reaction temperature was cooled to 90 °C for further precipitation and dispersion. After that, OAm-capped CISe QDs were obtained. The ligand transfer method was used to convert long-chain ligands (OAm) to short-chain ligands (MPA). After that, MPA-capped water-soluble CISe QDs were dispersed in 0.5 mL deionized water for spinning coating. The perovskite precursor was prepared by mixing MAI and  $\text{PbI}_2$  sources in 2-methoxyethanol (2ME) at the final concentration of 0.3 M.

**Fabrication Process of Photodetector:** Brand new ITO glasses were cleaned with deionized water, acetone, and alcohol at 30 °C for 20 min. The cleaned substrates were treated with UV-ozone for 10 min before using. The PEDOT:PSS was selected as the HTL and spin-coated on the ITO at 4000 rpm for 30s, and then annealed at 140 °C for 20 min. The MPA-CuInSe<sub>2</sub> QDs were spin-coated on the HTL at 2000 rpm for 20 s, and then annealed at 60 °C for 10 min. After that, MAPbI<sub>3</sub> perovskite films were spin-coated on the QDs layer by a one-step method at 4000 rpm for 30 s, and then the films were annealed at 60 °C for 1 min and 100 °C for 10 min. Then the PCBM layer was prepared by the spin-coating method at 2500 rpm for 30 s. Finally, the Ag electrode was deposited on the PCBM layer by thermal evaporation in a vacuum as the top electrode.

**Characterization:** The absorption and PL emission spectra were measured using an UV-vis spectrophotometer (Cary 5000, Varian) and a steady-state fluorescence spectrometer (DeltaFlex, HORIBA).

Jobinyvon IBH, Inc.), respectively. CISe QDs and perovskite were studied by X-ray diffraction with a Cu Ka wave. The cross-sectional SEM images of the perovskite were collected by cold field emission SEM (Hitachi S-4800). The STEM image of the CISe QDs was obtained on a FEI Titan Analytical 80-300ST TEM. The I-V curves of the devices were conducted on a digital source meter (2400, Keithley Instruments, Inc.) under 3 A grade AM 1.5G simulated sunlight ( $100 \text{ mW cm}^{-2}$ ) (7-SS1503A, 7 Star Optical Instruments Co., Beijing, China). The responsivity of the photodetector was measured in direct current mode using a custom measurement system consisting of a 150 W xenon lamp (7ILX150A, 7 Star Optical Instruments Co.), a monochromator (7ISW30, 7 Star Optical Instruments Co.), and a digital source meter (2400, Keithley Instruments, Inc.). The I-T curves were measured from an electrochemical workstation, light source (LED4, NBET-6500 K).

#### Acknowledgements

R.G. and C.B. contributed equally to this work. This work was supported by the National Natural Science Foundation of China (51961135107, 51774034, 51772026), National Key R&D Program of China (2017YFE0119700), and Beijing Natural Science Foundation (2182039). The authors thank J. Meng and Prof. K. Zheng of Technical University of Denmark for STEM measurements.

#### Conflict of Interest

The authors declare no conflict of interest.

## Keywords

broadband photodetectors, CuInSe<sub>2</sub> quantum dots, double active layers, perovskites, thermal stability

Received: March 31, 2020

Revised: May 9, 2020

Published online: May 26, 2020

- [1] C. Bao, J. Yang, S. Bai, W. Xu, Z. Yan, Q. Xu, J. Liu, W. Zhang, F. Gao, *Adv. Mater.* **2018**, *30*, 1803422.
- [2] R. Dong, Y. Fang, J. Chae, J. Dai, Z. Xiao, Q. Dong, Y. Yuan, A. Centrone, X. C. Zeng, J. Huang, *Adv. Mater.* **2015**, *27*, 1912.
- [3] W. Wang, D. Zhao, F. Zhang, L. Li, M. Du, C. Wang, Y. Yu, Q. Huang, M. Zhang, L. Li, J. Miao, Z. Lou, G. Shen, Y. Fang, Y. Yan, *Adv. Funct. Mater.* **2017**, *27*, 1703953.
- [4] X. Xiao, C. Bao, Y. Fang, J. Dai, B. R. Ecker, C. Wang, Y. Lin, S. Tang, Y. Liu, Y. Deng, X. Zheng, Y. Gao, X. C. Zeng, J. Huang, *Adv. Mater.* **2018**, *30*, 1705176.
- [5] W. Tian, H. Zhou, L. Li, *Small* **2017**, *13*, 1702107.
- [6] L. Ji, H.-Y. Hsu, J. C. Lee, A. J. Bard, E. T. Yu, *Nano Lett.* **2018**, *18*, 994.
- [7] F. Bai, J. Qi, F. Li, Y. Fang, W. Han, H. Wu, Y. Zhang, *Adv. Mater. Interfaces* **2018**, *5*, 1701275.
- [8] X. Hu, X. Zhang, L. Liang, J. Bao, S. Li, W. Yang, Y. Xie, *Adv. Funct. Mater.* **2014**, *24*, 7373.
- [9] Y. Wang, D. Yang, D. Ma, D. H. Kim, T. Ahamad, S. M. Alshehri, A. Vadim, *Sci. China Mater.* **2019**, *62*, 790.
- [10] M. M. Ackerman, X. Tang, P. Guyot-Sionnest, *ACS Nano* **2018**, *12*, 7264.
- [11] Z. Ren, J. Sun, H. Li, P. Mao, Y. Wei, X. Zhong, J. Hu, S. Yang, J. Wang, *Adv. Mater.* **2017**, *29*, 1702055.
- [12] M. Li, J.-S. Chen, P. K. Routh, P. Zahl, C.-Y. Nam, M. Cotlet, *Adv. Funct. Mater.* **2018**, *28*, 1707558.
- [13] F. E. S. Gorris, M. Deffner, S. Priyadarshi, C. Klinke, H. Weller, H. Lange, *Adv. Opt. Mater.* **2020**, *8*, 1901058.
- [14] J. Du, Z. Du, J. S. Hu, Z. Pan, Q. Shen, J. Sun, D. Long, H. Dong, L. Sun, X. Zhong, L. J. Wan, *J. Am. Chem. Soc.* **2016**, *138*, 4201.
- [15] M. G. Panthani, C. J. Stolle, D. K. Reid, D. J. Rhee, T. B. Harvey, V. A. Akhavan, Y. Yu, B. A. Korgel, *J. Phys. Chem. Lett.* **2013**, *4*, 2030.
- [16] R. Guo, T. Shen, J. Tian, *J. Mater. Chem. C* **2018**, *6*, 2573.
- [17] R. Guo, F. Huang, K. Zheng, T. Pullerits, J. Tian, *ACS Appl. Mater. Interfaces* **2018**, *10*, 35656.
- [18] W. Li, Z. Pan, X. Zhong, *J. Mater. Chem. A* **2015**, *3*, 1649.
- [19] G. Li, K. L. Ching, J. Y. L. Ho, M. Wong, H. Kwok, *Adv. Energy Mater.* **2015**, *5*, 1401775.
- [20] Y. Wu, X. Yang, W. Chen, Y. Yue, M. Cai, F. Xie, E. Bi, A. Islam, L. Han, *Nat. Energy* **2016**, *1*, 16148.
- [21] F. Tan, H. Tan, M. I. Saidaminov, M. Wei, M. Liu, A. Mei, P. Li, B. Zhang, C. Tan, X. Gong, Y. Zhao, A. R. Kirmani, Z. Huang, J. Z. Fan, R. Quintero-Bermudez, J. Kim, Y. Zhao, O. Vozny, Y. Gao, F. Zhang, L. J. Richter, Z. Lu, W. Zhang, E. H. Sargent, *Adv. Mater.* **2019**, *31*, 1807435.
- [22] W. Tian, L. Min, F. Cao, L. Li, *Adv. Mater.* **2020**, *32*, 1906974.
- [23] M. Li, B. Li, G. Cao, J. Tian, *J. Mater. Chem. A* **2017**, *5*, 21313.
- [24] T. Shen, B. Li, K. Zheng, T. Pullerits, G. Cao, J. Tian, *J. Phys. Chem. Lett.* **2018**, *9*, 3285.
- [25] J. Yuan, L. Zhang, C. Bi, M. Wang, J. Tian, *Sol. RRL* **2018**, *2*, 1800188.
- [26] J. Yuan, C. Bi, S. Wang, R. Guo, T. Shen, L. Zhang, J. Tian, *Adv. Funct. Mater.* **2019**, *29*, 1906615.
- [27] M. Wang, F. Gao, K. Deng, L. Li, *Nano Energy* **2019**, *63*, 103867.
- [28] L. Shen, Y. Lin, C. Bao, Y. Bai, Y. Deng, M. Wang, T. Li, Y. Lu, A. Gruber, W. Li, J. Huang, *Mater. Horiz.* **2017**, *4*, 242.
- [29] Y. Wei, Z. Ren, A. Zhang, P. Mao, H. Li, X. Zhong, W. Li, S. Yang, J. Wang, *Adv. Funct. Mater.* **2018**, *28*, 1706690.
- [30] Y. Fang, J. Huang, *Adv. Mater.* **2015**, *27*, 2804.
- [31] B. Yang, F. Zhang, J. Chen, S. Yang, X. Xia, T. Pullerits, W. Deng, K. Han, *Adv. Mater.* **2017**, *29*, 1703758.
- [32] R. Guo, L. Zhang, J. Meng, A. Liu, J. Yuan, K. Zheng, J. Tian, *Adv. Electron. Mater.* **2020**, *6*, 2000035.